








ARTICLE

DOI: 10.1038/s41467-018-03266-0

OPEN

Direct observation of orbital hybridisation in a cuprate superconductor

C.E. Matt ^{1,2}, D. Sutter ¹, A.M. Cook¹, Y. Sassa³, M. Månsson ⁴, O. Tjernberg ⁴, L. Das¹, M. Horio ¹, D. Destraz¹, C.G. Fatuzzo⁵, K. Hauser¹, M. Shi², M. Kobayashi², V.N. Strocov², T. Schmitt², P. Dudin⁶, M. Hoesch⁶, S. Pyon⁷, T. Takayama⁷, H. Takagi ⁷, O.J. Lipscombe⁸, S.M. Hayden⁸, T. Kurosawa⁹, N. Momono^{9,10}, M. Oda⁹, T. Neupert¹ & J. Chang ¹

The minimal ingredients to explain the essential physics of layered copper-oxide (cuprates) materials remains heavily debated. Effective low-energy single-band models of the copper-oxygen orbitals are widely used because there exists no strong experimental evidence supporting multi-band structures. Here, we report angle-resolved photoelectron spectroscopy experiments on La-based cuprates that provide direct observation of a two-band structure. This electronic structure, qualitatively consistent with density functional theory, is parametrised by a two-orbital ($d_{x^2-y^2}$ and d_{z^2}) tight-binding model. We quantify the orbital hybridisation which provides an explanation for the Fermi surface topology and the proximity of the van-Hove singularity to the Fermi level. Our analysis leads to a unification of electronic hopping parameters for single-layer cuprates and we conclude that hybridisation, restraining d -wave pairing, is an important optimisation element for superconductivity.

¹Physik-Institut, Universität Zürich, Winterthurerstrasse 190, CH-8057 Zürich, Switzerland. ²Swiss Light Source, Paul Scherrer Institut, CH-5232 Villigen PSI, Switzerland. ³Department of Physics and Astronomy, Uppsala University, SE-75121 Uppsala, Sweden. ⁴Materials Physics, KTH Royal Institute of Technology, SE-164 40 Kista, Stockholm, Sweden. ⁵Institute of Physics, École Polytechnique Fédérale de Lausanne (EPFL), Lausanne CH-1015, Switzerland. ⁶Diamond Light Source, Harwell Campus, Didcot OX11 0DE, UK. ⁷Department of Advanced Materials, University of Tokyo, Kashiwa 277-8561, Japan. ⁸H. H. Wills Physics Laboratory, University of Bristol, Bristol BS8 1TL, UK. ⁹Department of Physics, Hokkaido University, Sapporo 060-0810, Japan. ¹⁰Department of Applied Sciences, Muroran Institute of Technology, Muroran 050-8585, Japan. Correspondence and requests for materials should be addressed to C.E.M. (email: cmatt@g.harvard.edu) or to J.C. (email: johan.chang@physik.uzh.ch)

Identifying the factors that limit the transition temperature T_c of high-temperature cuprate superconductivity is a crucial step towards revealing the design principles underlying the pairing mechanism¹. It may also provide an explanation for the dramatic variation of T_c across the known single-layer compounds². Although superconductivity is certainly promoted within the copper-oxide layers, the apical oxygen position may play an important role in defining the transition temperature^{3–7}. The CuO_6 octahedron lifts the degeneracy of the nine copper $3d$ -electrons and generates fully occupied t_{2g} and $3/4$ -filled e_g states⁸. With increasing apical oxygen distance d_A to the CuO_2 plane, the e_g states split to create a $1/2$ -filled $d_{x^2-y^2}$ band. The distance d_A thus defines whether single or two-band models are most appropriate to describe the low-energy band structure. It has also been predicted that d_A influences T_c in at least two different ways. First, the distance d_A controls the charge transfer gap between the oxygen and copper site which, in turn, suppresses superconductivity^{5,9}. Second, Fermi-level d_{z^2} hybridisation, depending on d_A , reduces the pairing strength^{6,10}. Experimental evidence, however, points in opposite directions. Generally, single-layer materials with larger d_A have indeed a larger T_c ². However, scanning tunneling microscopy (STM) studies of Bi-based cuprates suggest an anti-correlation between d_A and T_c ¹¹.

In the quest to disentangle these causal relation between d_A and T_c , it is imperative to experimentally reveal the orbital character of the cuprate band structure. The comparably short apical oxygen distance d_A makes $\text{La}_{2-x}\text{Sr}_x\text{CuO}_4$ (LSCO) an ideal candidate for such a study. Experimentally, however, it is challenging to determine the orbital character of the states near the Fermi energy (E_F). In fact, the d_{z^2} band has never been identified directly by angle-resolved photoelectron spectroscopy (ARPES) experiments. A large majority of ARPES studies have focused on the pseudogap, superconducting gap and quasi-particle self-energy properties in near vicinity to the Fermi level¹². An exception to this trend are studies of the so-called

waterfall structure^{13–17} that lead to the observation of band structures below the $d_{x^2-y^2}$ band^{14,16}. However, the origin and hence orbital character of these bands was never addressed. Resonant inelastic X-ray scattering has been used to probe excitations between orbital d -levels. In this fashion, insight about the position of d_{z^2} , d_{xz} , d_{yz} and d_{xy} states with respect to $d_{x^2-y^2}$ has been obtained¹⁸. Although difficult to disentangle, it has been argued that for LSCO the d_{z^2} level is found above d_{xz} , d_{yz} and d_{xy} ^{19,20}. To date, a comprehensive study of the d_{z^2} momentum dependence is missing and therefore the coupling between the d_{z^2} and $d_{x^2-y^2}$ bands has not been revealed. X-ray absorption spectroscopy (XAS) experiments, sensitive to the unoccupied states, concluded only marginal hybridisation of $d_{x^2-y^2}$ and d_{z^2} states in LSCO²¹. Therefore, the role of d_{z^2} hybridisation remains ambiguous²².

Here we provide direct ultraviolet and soft-X-ray ARPES measurements of the d_{z^2} band in La-based single-layer compounds. The d_{z^2} band is located about 1 eV below the Fermi level at the Brillouin zone (BZ) corners. From these corners, the d_{z^2} band is dispersing downwards along the nodal and anti-nodal directions, consistent with density functional theory (DFT) calculations. The experimental and DFT band structure, including only $d_{x^2-y^2}$ and d_{z^2} orbitals, is parametrised using a two-orbital tight-binding model²³. The presence of the d_{z^2} band close to the Fermi level allows to describe the Fermi surface topology for all single-layer compounds (including $\text{HgBa}_2\text{CuO}_{4+x}$ and $\text{Tl}_2\text{Ba}_2\text{CuO}_{6+x}$) with similar hopping parameters for the $d_{x^2-y^2}$ orbital. This unification of electronic parameters implies that the main difference between single-layer cuprates originates from the hybridisation between $d_{x^2-y^2}$ and d_{z^2} orbitals. The significantly increased hybridisation in La-based cuprates pushes the van-Hove singularity close to the Fermi level. This explains why the Fermi surface differs from other single-layer compounds. We directly quantify the orbital hybridisation that plays a sabotaging role for superconductivity.

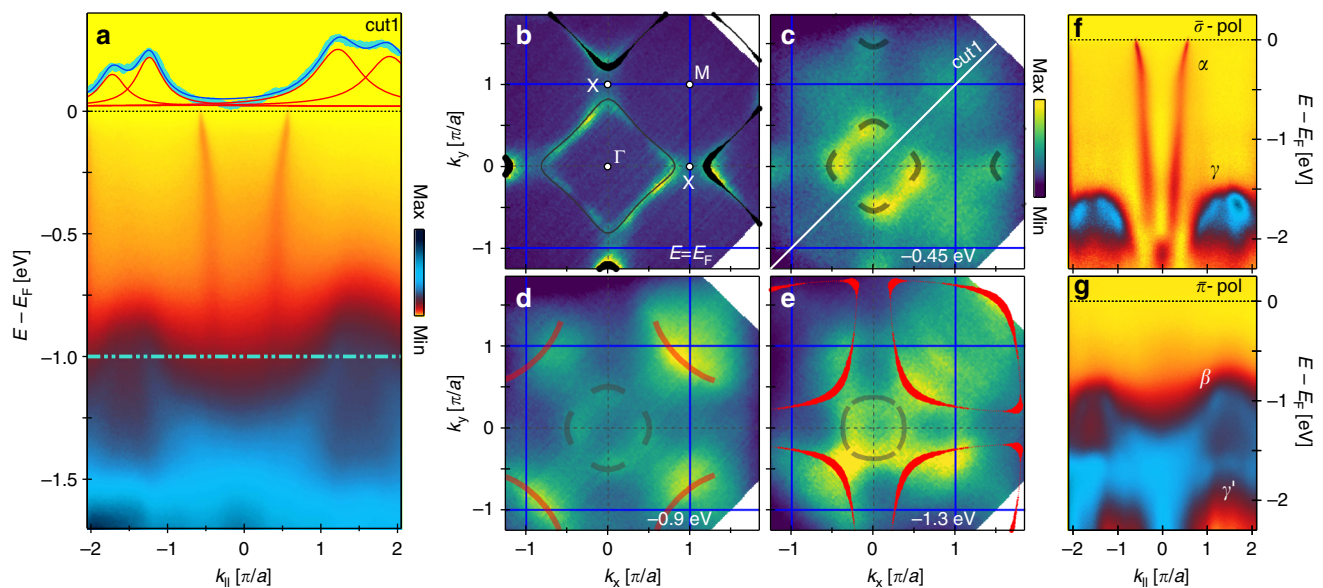


Fig. 1 ARPES spectra showing e_g -bands of overdoped $\text{La}_{2-x}\text{Sr}_x\text{CuO}_{4-x=0.23}$. **a** Raw ARPES energy distribution map (EDM) along cut 1 as indicated in **(c)**. Dashed green line indicates the position of MDC displayed on top by turquoise circles. A linear background has been subtracted from the MDC which is fitted (blue line) by four Lorentzians (red lines). **b–e** Constant binding energy maps at E_F (**b**) and at higher binding energies (**c–e**) as indicated. The photoemission intensity, shown in false colour scale, is integrated over ± 10 meV. Black (red) lines indicate the position of $d_{x^2-y^2}$ (d_{z^2}) bands. The curve thickness in **b, e** is scaled to the contribution of the d_{z^2} orbital. Semitransparent lines are guides to the eye. **f, g** EDMs along cut 1 recorded with $\bar{\sigma}$ and $\bar{\pi}$ light, **f** sensitive to the low-energy $d_{x^2-y^2}$ and d_{xz}/d_{yz} bands and **g** the d_{z^2} and d_{xy} -derived bands. All data have been recorded with $h\nu = 160$ eV

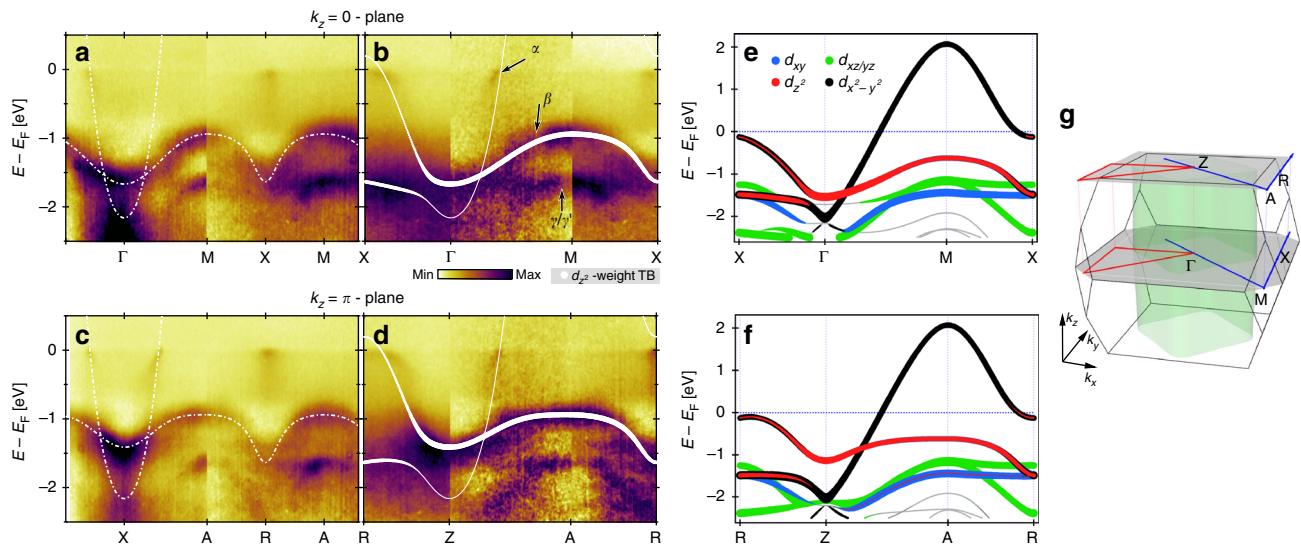


Fig. 2 Comparison of observed and calculated band structure. **a–d** Background subtracted (see Methods section) soft-X-ray ARPES EDMs recorded on $\text{La}_{2-x}\text{Sr}_x\text{CuO}_4$, $x = 0.23$ along in-plane high-symmetry directions for $k_z = 0$ and $k_z = \pi/c'$ as indicated in **g**. White lines represent the two-orbital (d_{z^2} and $d_{x^2-y^2}$) tight-binding model as described in the text. The line width in **b, d** indicates the orbital weight of the d_{z^2} orbital. **e, f** Corresponding in-plane DFT band structure at $k_z = 0$ and $k_z = \pi/c'$, calculated for La_2CuO_4 (see Methods section). The colour code indicates the orbital character of the bands. Around the anti-nodal points (X or R), strong hybridisation of d_{z^2} and $d_{x^2-y^2}$ orbitals is found. In contrast, symmetry prevents any hybridisation along the nodal lines (Γ -M or Z-A). **g** Sketch of the 3D BZ of LSCO with high symmetry lines and points as indicated

Results

Material choices. Different dopings of LSCO spanning from $x = 0.12$ to 0.23 in addition to an overdoped compound of $\text{La}_{1.8-x}\text{Eu}_{0.2}\text{Sr}_x\text{CuO}_4$ with $x = 0.21$ have been studied. These compounds represent different crystal structures: low-temperature orthorhombic, low-temperature tetragonal and the high-temperature tetragonal. Our results are very similar across all crystal structures and dopings (Supplementary Fig. 1). To keep the comparison to band structure calculations simple, this paper focuses on results obtained in the tetragonal phase of overdoped LSCO with $x = 0.23$.

Electronic band structure. A raw ARPES energy distribution map (EDM), along the nodal direction, is displayed in Fig. 1a. Near E_F , the widely studied nodal quasiparticle dispersion with predominately $d_{x^2-y^2}$ character is observed¹². This band reveals the previously reported electron-like Fermi surface of LSCO, $x = 0.23$ ^{24,25} (Fig. 1b), the universal nodal Fermi velocity $v_F \approx 1.5 \text{ eV\AA}^{26}$ and a band dispersion kink around 70 meV^{26} . The main observation reported here is the second band dispersion at $\sim 1 \text{ eV}$ below the Fermi level E_F (Figs. 1 and 2) and a hybridisation gap splitting the two (Fig. 3). This second band—visible in both raw momentum distribution curves (MDC) and constant energy maps—disperses downwards away from the BZ corners. Since a pronounced k_z dependence is observed for this band structure (Figs. 2 and 4) a trivial surface state can be excluded. Subtracting a background intensity profile (Supplementary Fig. 2) is a standard method that enhances visualisation of this second band structure. In fact, using soft X-rays (160–600 eV), at least two additional bands (β and γ) are found below the $d_{x^2-y^2}$ dominated band crossing the Fermi level. Here, focus is set entirely on the β band dispersion closest to the $d_{x^2-y^2}$ dominated band. This band is clearly observed at the BZ corners (Figs. 1–3). The complete in-plane (k_x, k_y) and out-of-plane (k_z) band dispersion is presented in Fig. 4.

Orbital band characters. To gain insight into the orbital character of these bands, a comparison with a DFT band structure

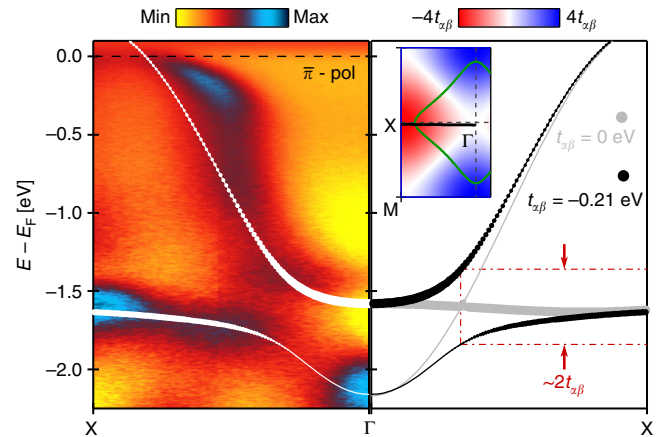


Fig. 3 Avoided band crossing. Left panel: ultraviolet ARPES data recorded along the anti-nodal direction using 160 eV linear horizontal polarised photons. Solid white lines are the same tight-binding model as shown in Fig. 2. Right panel: tight-binding model of the $d_{x^2-y^2}$ and d_{z^2} bands along the anti-nodal direction. Grey lines are the model prediction in absence of inter-orbital hopping ($t_{\alpha\beta} = 0$) between $d_{x^2-y^2}$ and d_{z^2} . In this case, the bands are crossing near the Γ -point. This degeneracy is lifted once a finite inter-orbital hopping parameter is considered. For solid black lines $t_{\alpha\beta} = -210 \text{ meV}$ and other hopping parameters have been adjusted accordingly. Inset indicates the Fermi surface (green line) and the $\Gamma - X$ cut directions. Coloured background displays the amplitude of the hybridisation term $\Psi(\mathbf{k})$ that vanishes on the nodal lines

calculation (see Methods section) of La_2CuO_4 is shown in Fig. 2. The e_g states ($d_{x^2-y^2}$ and d_{z^2}) are generally found above the t_{2g} bands (d_{xy} , d_{xz} and d_{yz}). The overall agreement between the experiment and the DFT calculation (Supplementary Fig. 3) thus suggests that the two bands nearest to the Fermi level are composed predominately of $d_{x^2-y^2}$ and d_{z^2} orbitals. This conclusion can also be reached by pure experimental arguments. Photoemission matrix element selection rules contain information

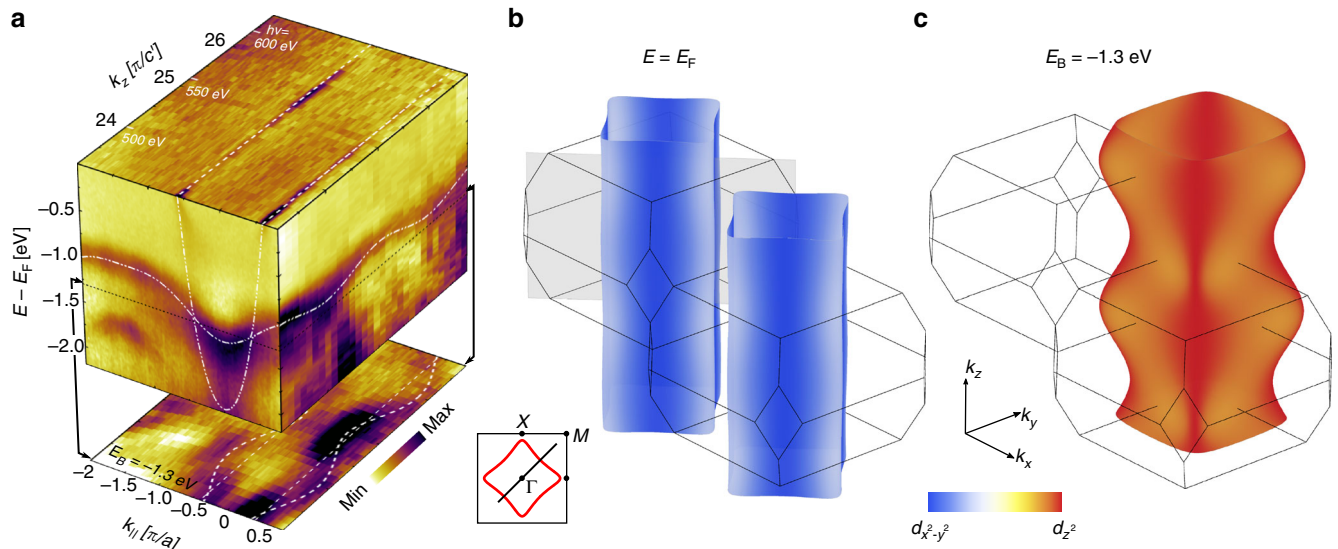


Fig. 4 Three-dimensional band dispersion. **a** k_z dispersion recorded along the diagonal (π, π) direction of the $d_{x^2-y^2}$ and d_{z^2} bands (along grey plane in **b**). Whereas the $d_{x^2-y^2}$ band displays no k_z dependence beyond matrix element effects, the d_{z^2} band displays a discernible k_z dispersion. The iso-energy map below the cube has binding energy $E - E_F = -1.3$ eV. White lines represent the tight-binding model. **b, c** Tight-binding representation of the Fermi surface (α band) and iso-energy surface (-1.3 eV) of the β band. The colour code indicates the \mathbf{k} -dependent orbital hybridisation. The orbital hybridisation at E_F is largest in the anti-nodal region of the $k_z = \pi/c'$ plane where the d_{z^2} admixture at k_F amounts to $\sim 1/3$

Table 1 Tight-binding parameters for single-layer cuprate materials

Compound	LSCO	Hg1201	Tl2201	LSCO
Doping p	0.22	0.16	0.26	0.23
Tight binding parameters in units of $t_\alpha = -1.21$ eV				
$-\mu$	0.88	1.27	1.35	0.96
$-t'_\alpha$	0.13	0.47	0.42	0.32
t''_α	0.065	0.02	0.02	0.0
$t_{\alpha\beta}$	0	0	0	0.175
t'_β	-	-	-	0.062
t''_β	-	-	-	0.017
$t_{\beta z}$	-	-	-	0.017
$-t'_{\beta z}$	-	-	-	0.0017
Ref.	24	39,40	41,42	This work

Comparison of tight-binding hopping parameters obtained from single-orbital and two-orbital models. Once a coupling $t_{\alpha\beta}$ between the $d_{x^2-y^2}$ and d_{z^2} band is introduced for $\text{La}_{2-x}\text{Sr}_x\text{CuO}_4$, the $d_{x^2-y^2}$ hopping parameters become comparable to those of Hg1201 and Tl2201

about the orbital band character. They can be probed in a particular experimental setup where a mirror-plane is defined by the incident light and the electron analyser slit¹². With respect to this plane the electromagnetic light field has odd (even) parity for $\bar{\sigma}$ ($\bar{\pi}$) polarisation (Supplementary Fig. 4). Orienting the mirror plane along the nodal direction (cut 1 in Fig. 1), the d_{z^2} and d_{xy} ($d_{x^2-y^2}$) orbitals have even (odd) parity. For a final-state with even parity, selection rules¹² dictate that the d_{z^2} and d_{xy} -derived bands should appear (vanish) in the $\bar{\pi}$ ($\bar{\sigma}$) polarisation channel and vice versa for $d_{x^2-y^2}$. Due to their orientation in real-space, the d_{xz} and d_{yz} orbitals are not expected to show a strict switching behaviour along the nodal direction²⁷. As shown in Fig. 1f, g, two bands (α and γ) appear with $\bar{\sigma}$ -polarised light while for $\bar{\pi}$ -polarised light bands β and γ' are observed. Band α which crosses E_F is assigned to $d_{x^2-y^2}$ while band γ has to originate from d_{xz}/d_{yz} orbitals as d_{z^2} and d_{xy} -derived states are fully suppressed for $\bar{\sigma}$ -polarised light. In the EDM, recorded with $\bar{\pi}$ -polarised light, band (β) at ~ 1 eV binding energy and again a band (γ') at ~ 1.6 eV

is observed. From the orbital shape, a smaller k_z dispersion is expected for $d_{x^2-y^2}$ and d_{xy} -derived bands than for those from d_{z^2} orbitals. As the β band exhibits a significant k_z dispersion (Fig. 4), much larger than observed for the $d_{x^2-y^2}$ band, we conclude that it is of d_{z^2} character. The γ' band which is very close to the γ band is therefore of d_{xy} character. Interestingly, this d_{z^2} -derived band has stronger in-plane than out-of-plane dispersion, suggesting that there is a significant hopping to in-plane p_x and p_y oxygen orbitals. Therefore the assumption that the d_{z^2} states are probed uniquely through the apical oxygen p_z orbital²¹ has to be taken with caution.

Discussion

Most minimal models aiming to describe the cuprate physics start with an approximately half-filled single $d_{x^2-y^2}$ band on a two-dimensional square lattice. Experimentally, different band structures have been observed across single-layer cuprate compounds. The Fermi surface topology of LSCO is, for example, less rounded compared to $(\text{Bi,Pb})_2(\text{Sr,La})_2\text{CuO}_{6+x}$ (Bi2201), $\text{Tl}_2\text{Ba}_2\text{CuO}_{6+x}$ (Tl2201) and $\text{HgBa}_2\text{CuO}_{4+x}$ (Hg1201). Within a single-band tight-binding model the rounded Fermi surface shape of the single-layer compounds Hg1201 and Tl2201 is described by setting $r = (|t'_\alpha| + |t''_\alpha|)/t_\alpha \sim 0.4$ ⁶, where t_α , t'_α and t''_α are nearest neighbour (NN), next-nearest neighbour (NNN) and next-next-nearest neighbour (NNNN) hopping parameters (Table 1 and Supplementary Fig. 4). For LSCO with more flat Fermi surface sections, significantly lower values of r have been reported. For example, for overdoped $\text{La}_{1.78}\text{Sr}_{0.22}\text{CuO}_4$, $r \sim 0.2$ was found^{24,25}. The single-band premise thus leads to varying hopping parameters across the cuprate families, stimulating the empirical observation that T_c^{max} roughly scales with t'_α ². This, however, is in direct contrast to t - J models that predict the opposite correlation^{28,29}. Thus the single-band structure applied broadly to all single-layer cuprates lead to conclusions that challenge conventional theoretical approaches.

The observation of the d_{z^2} band calls for a re-evaluation of the electronic structure in La-based cuprates using a two-orbital

tight-binding model (see Methods section). Crucially, there is a hybridisation term $\Psi(\mathbf{k}) = 2t_{\alpha\beta}[\cos(k_x a) - \cos(k_y b)]$ between the $d_{x^2-y^2}$ and d_{z^2} orbitals, where $t_{\alpha\beta}$ is a hopping parameter that characterises the strength of orbital hybridisation. In principle, one may attempt to describe the two observed bands independently by taking $t_{\alpha\beta} = 0$. However, the problem then returns to the single-band description with the above mentioned contradictions. Furthermore, $t_{\alpha\beta} = 0$ implies a band crossing in the anti-nodal direction that is not observed experimentally (Fig. 3). In fact, from the avoided band crossing one can directly estimate $t_{\alpha\beta} \approx -200$ meV. As dictated by the different eigenvalues of the orbitals under mirror symmetry, the hybridisation term $\Psi(\mathbf{k})$ vanishes on the nodal lines $k_x = \pm k_y$ (see inset of Fig. 3). Hence the pure $d_{x^2-y^2}$ and d_{z^2} orbital band character is expected along these nodal lines. The hybridisation $\Psi(\mathbf{k})$ is largest in the anti-nodal region, pushing the van-Hove singularity of the upper band close to the Fermi energy and in case of overdoped LSCO across the Fermi level.

In addition to the hybridisation parameter $t_{\alpha\beta}$ and the chemical potential μ , six free parameters enter the tight-binding model that yields the entire band structure (white lines in Figs. 2 and 4). Nearest and next-nearest in-plane hopping parameters between $d_{x^2-y^2}$ (t_α, t'_α) and d_{z^2} (t_β, t'_β) orbitals are introduced to capture the Fermi surface topology and in-plane d_{z^2} band dispersion (Supplementary Fig. 4). The k_z dispersion is described by nearest and next-nearest out-of-plane hoppings ($t_{\beta z}, t'_{\beta z}$) of the d_{z^2} orbital. The four d_{z^2} hopping parameters and the chemical potential μ are determined from the experimental band structure along the nodal direction where $\Psi(\mathbf{k}) = 0$. Furthermore, the α and β band dispersion in the anti-nodal region and the Fermi surface topology provide the parameters t_α, t'_α and $t_{\alpha\beta}$. Our analysis reveals a finite band coupling $t_{\alpha\beta} = -0.21$ eV resulting in a strong anti-nodal orbital hybridisation (Fig. 2 and Table 1). Compared to the single-band parametrisation²⁴ a significantly larger value $r \sim -0.32$ is found and hence a unification of t'_α/t_α ratios for all single-layer compounds is achieved.

Finally, we discuss the implication of orbital hybridisation for superconductivity and pseudogap physics. First, we notice that a pronounced pseudogap is found in the anti-nodal region of $\text{La}_{1.8-x}\text{Eu}_{0.2}\text{Sr}_x\text{CuO}_4$ with $x = 0.21$ —consistent with transport experiments³⁰ (Supplementary Fig. 5). The fact that $t_{\alpha\beta}$ of $\text{La}_{1.59}\text{Eu}_{0.2}\text{Sr}_{0.21}\text{CuO}_4$ is similar to $t_{\alpha\beta}$ of LSCO suggests that the pseudogap is not suppressed by the d_{z^2} hybridisation. To this end, a comparison to the 1/4-filled e_g system $\text{Eu}_{2-x}\text{Sr}_x\text{NiO}_4$ with $x = 1.1$ is interesting^{31,32}. This material has the same two-orbital band structure with protection against hybridisation along the nodal lines. Both the $d_{x^2-y^2}$ and d_{z^2} bands are crossing the Fermi level, producing two Fermi surface sheets³¹. Despite an even stronger d_{z^2} admixture of the $d_{x^2-y^2}$ derived band a d -wave-like pseudogap has been reported³². The pseudogap physics thus seems to be unaffected by the orbital hybridisation.

It has been argued that orbital hybridisation—of the kind reported here—is unfavourable for superconducting pairing^{6,10}. It thus provides an explanation for the varying T_c^{max} across single-layer cuprate materials. Although other mechanisms, controlled by the apical oxygen distance, (e.g. variation of the copper–oxygen charge transfer gap⁴) are not excluded our results demonstrate that orbital hybridisation exists and is an important control parameter for superconductivity.

Methods

Sample characterisation. High-quality single crystals of LSCO, $x = 0.12, 0.23$, and $\text{La}_{1.8-x}\text{Eu}_{0.2}\text{Sr}_x\text{CuO}_4$, $x = 0.21$, were grown by the floating-zone technique. The samples were characterised by SQUID magnetisation³³ to determine superconducting transition temperatures ($T_c = 27, 24$ and 14 K). For the crystal structure, the experimental lattice parameters are $a = b = 3.78$ Å and $c = 2c' = 13.2$ Å³⁴.

ARPES experiments. Ultraviolet and soft-X-ray ARPES experiments were carried out at the SIS⁴³ and ADDRESS⁴⁴ beam-lines at the Swiss Light Source and at the I05 beamline at Diamond Light Source. Samples were pre-aligned ex situ using a X-ray LAUE instrument and cleaved in situ—at base temperature (10–20 K) and ultra high vacuum ($\leq 5 \times 10^{-11}$ mbar)—employing a top-post technique or cleaving device³⁵. Ultraviolet (soft X-ray³⁶) ARPES spectra were recorded using a SCIENTA R4000 (SPECS PHOIBOS-150) electron analyser with horizontal (vertical) slit setting. All data was recorded at the cleaving temperature 10–20 K. To visualise the d_{z^2} -dominated band, we subtracted in Fig. 1f, g and Figs. 2–4 the background that was obtained by taking the minimum intensity of the MDC at each binding energy.

Tight-binding model. A two-orbital tight-binding model Hamiltonian with symmetry-allowed hopping terms is employed to isolate and characterise the extent of orbital hybridisation of the observed band structure²³. For compactness of the momentum-space Hamiltonian matrix representation, we introduce the vectors

$$\begin{aligned} \mathbf{Q}^\kappa &= (a, \kappa b, 0)^\top, \\ \mathbf{R}^{\kappa_1, \kappa_2} &= (\kappa_1 a, \kappa_1 \kappa_2 b, c)^\top / 2, \\ \mathbf{T}_1^{\kappa_1, \kappa_2} &= (3\kappa_1 a, \kappa_1 \kappa_2 b, c)^\top / 2, \\ \mathbf{T}_2^{\kappa_1, \kappa_2} &= (\kappa_1 a, 3\kappa_1 \kappa_2 b, c)^\top / 2, \end{aligned} \quad (1)$$

where κ, κ_1 and κ_2 take values ± 1 as defined by sums in the Hamiltonian and \top denotes vector transposition.

Neglecting the electron spin (spin–orbit coupling is not considered) the momentum-space tight-binding Hamiltonian, $\mathcal{H}(\mathbf{k})$, at a particular momentum $\mathbf{k} = (k_x, k_y, k_z)$ is then given by

$$\mathcal{H}(\mathbf{k}) = \begin{bmatrix} M^{x^2-y^2}(\mathbf{k}) & \Psi(\mathbf{k}) \\ \Psi(\mathbf{k}) & M^{z^2}(\mathbf{k}) \end{bmatrix}, \quad (2)$$

in the basis $(c_{\mathbf{k}, x^2-y^2}, c_{\mathbf{k}, z^2})^\top$, where the operator $c_{\mathbf{k}, \alpha}$ annihilates an electron with momentum \mathbf{k} in an e_g -orbital d_α , with $\alpha \in \{x^2-y^2, z^2\}$. The diagonal matrix entries are given by

$$\begin{aligned} M^{x^2-y^2}(\mathbf{k}) &= 2t_\alpha [\cos(k_x a) + \cos(k_y b)] + \mu \\ &+ \sum_{\kappa=\pm 1} 2t'_\alpha \cos(\mathbf{Q}^\kappa \cdot \mathbf{k}) \\ &+ 2t''_\alpha [\cos(2k_x a) + \cos(2k_y b)], \end{aligned} \quad (3)$$

and

$$\begin{aligned} M^{z^2}(\mathbf{k}) &= 2t_\beta [\cos(k_x a) + \cos(k_y b)] - \mu \\ &+ \sum_{\kappa=\pm 1} 2t'_\beta \cos(\mathbf{Q}^\kappa \cdot \mathbf{k}) \\ &+ \sum_{\kappa_{1,2}=\pm 1} [2t_{\beta z} \cos(\mathbf{R}^{\kappa_1, \kappa_2} \cdot \mathbf{k}) \\ &+ \sum_{i=1,2} 2t'_{\beta z} \cos(\mathbf{T}_i^{\kappa_1, \kappa_2} \cdot \mathbf{k})], \end{aligned} \quad (4)$$

which describe the intra-orbital hopping for $d_{x^2-y^2}$ and d_{z^2} orbitals, respectively. The inter-orbital nearest-neighbour hopping term is given by

$$\Psi(\mathbf{k}) = 2t_{\alpha\beta} [\cos(k_x a) - \cos(k_y b)]. \quad (5)$$

In the above, μ determines the chemical potential. The hopping parameters t_α, t'_α and t''_α characterise NN, NNN and NNNN intra-orbital in-plane hopping between $d_{x^2-y^2}$ orbitals. t_β and t'_β characterise NN and NNN intra-orbital in-plane hopping between d_{z^2} orbitals, while $t_{\beta z}$ and $t'_{\beta z}$ characterise NN and NNN intra-orbital out-of-plane hopping between d_{z^2} orbitals, respectively (Supplementary Fig. 3). Finally, the hopping parameter $t_{\alpha\beta}$ characterises NN inter-orbital in-plane hopping. Note that in our model, $d_{x^2-y^2}$ intraorbital hopping terms described by the vectors (Eq. (1)) are neglected as these are expected to be weak compared to those of the d_{z^2} orbital. This is due to the fact that the inter-plane hopping is mostly mediated by hopping between apical oxygen p_z orbitals, which in turn only hybridise with the d_{z^2} orbitals, not with the $d_{x^2-y^2}$ orbitals. Such an argument highlights that the tight-binding model is not written in atomic orbital degrees of freedom, but in Wannier orbitals, which are formed from the Cu d orbitals and the ligand oxygen p orbitals. As follows from symmetry considerations and is discussed in ref. 10, the Cu d_{z^2} orbital together with the apical oxygen p_z orbital forms a Wannier orbital with d_{z^2} symmetry, while the Cu $d_{x^2-y^2}$ orbital together with the four neighbouring p_σ orbitals of the in-plane oxygen forms a Wannier orbital with $d_{x^2-y^2}$ symmetry. One should thus think of this tight-binding model as written in terms of these Wannier orbitals, thus implicitly containing superexchange hopping via the ligand oxygen p orbitals. Additionally we stress that all hopping parameters effectively include the oxygen orbitals. Diagonalising Hamiltonian (2), we find two

bands

$$\varepsilon_{\pm}(\mathbf{k}) = \frac{1}{2} [M^{x^2-y^2}(\mathbf{k}) + M^z(\mathbf{k}) \pm \frac{1}{2} \sqrt{[M^{x^2-y^2}(\mathbf{k}) - M^z(\mathbf{k})]^2 + 4\Psi^2(\mathbf{k})}], \quad (6)$$

and make the following observations: along the $k_x = \pm k_y$ lines, $\Psi(\mathbf{k})$ vanishes and hence no orbital mixing appears in the nodal directions. The reason for this absence of mixing lies in the different mirror eigenvalues of the two orbitals involved. Hence it is not an artifact of the finite range of hopping processes included in our model. The parameters of the tight-binding model are determined by fitting the experimental band structure and are provided in Table 1.

DFT calculations. DFT calculations were performed for La_2CuO_4 in the tetragonal space group $I4/mmm$, No. 139, found in the overdoped regime of LSCO using the WIEN2K package³⁷. Atomic positions are those inferred from neutron diffraction measurements³⁴ for $x = 0.225$. In the calculation, the Kohn–Sham equation is solved self-consistently by using a full-potential linear augmented plane wave (LAPW) method. The self-consistent field calculation converged properly for a uniform k -space grid in the irreducible BZ. The exchange–correlation term is treated within the generalised gradient approximation in the parametrisation of Perdew, Burke and Enzerhof³⁸. The plane wave cutoff condition was set to $RK_{\text{max}} = 7$ where R is the radius of the smallest LAPW sphere (i.e. 1.63 times the Bohr radius) and K_{max} denotes the plane wave cutoff.

Data availability. All experimental data are available upon request to the corresponding authors.

Received: 21 August 2017 Accepted: 1 February 2018

Published online: 06 March 2018

References

- Lee, P. A., Nagaosa, N. & Wen, X.-G. Doping a Mott insulator: physics of high-temperature superconductivity. *Rev. Mod. Phys.* **78**, 17–85 (2006).
- Pavarini, E. et al. Band-structure trend in hole-doped cuprates and correlation with T_{cmax} . *Phys. Rev. Lett.* **87**, 047003 (2001).
- Ohta, Y., Tohyama, T. & Maekawa, S. Apex oxygen and critical temperature in copper oxide superconductors: universal correlation with the stability of local singlets. *Phys. Rev. B* **43**, 2968–2982 (1991).
- Weber, C. et al. Orbital currents in extended hubbard models of high- T_c cuprate superconductors. *Phys. Rev. Lett.* **102**, 017005 (2009).
- Weber, C., Haule, K. & Kotliar, G. Apical oxygens and correlation strength in electron- and hole-doped copper oxides. *Phys. Rev. B* **82**, 125107 (2010).
- Sakakibara, H. et al. Two-orbital model explains the higher transition temperature of the single-layer Hg-cuprate superconductor compared to that of the La-cuprate superconductor. *Phys. Rev. Lett.* **105**, 057003 (2010).
- Raimondi, R., Jefferson, J. H. & Feiner, L. F. Effective single-band models for the high- T_c cuprates. II. Role of apical oxygen. *Phys. Rev. B* **53**, 8774–8788 (1996).
- Fink, J. et al. Electronic structure studies of high- T_c superconductors by high-energy spectroscopies. *IBM J. Res. Dev.* **33**, 372 (1989).
- Ruan, W. et al. Relationship between the parent charge transfer gap and maximum transition temperature in cuprates. *Sci. Bull.* **61**, 1826–1832 (2016).
- Sakakibara, H. et al. Origin of the material dependence of T_c in the single-layered cuprates. *Phys. Rev. B* **85**, 064501 (2012).
- Slezak, J. A. et al. Imaging the impact on cuprate superconductivity of varying the interatomic distances within individual crystal unit cells. *Proc. Natl. Acad. Sci. USA* **105**, 3203–3208 (2008).
- Damascelli, A., Hussain, Z. & Shen, Z.-X. Angle-resolved photoemission studies of the cuprate superconductors. *Rev. Mod. Phys.* **75**, 473–541 (2003).
- Graf, J. et al. Universal high energy anomaly in the angle-resolved photoemission spectra of high temperature superconductors: possible evidence of spinon and holon branches. *Phys. Rev. Lett.* **98**, 067004 (2007).
- Xie, B. P. et al. High-energy scale revival and giant kink in the dispersion of a cuprate superconductor. *Phys. Rev. Lett.* **98**, 147001 (2007).
- Valla, T. et al. High-energy kink observed in the electron dispersion of high-temperature cuprate superconductors. *Phys. Rev. Lett.* **98**, 167003 (2007).
- Meevasana, W. et al. Hierarchy of multiple many-body interaction scales in high-temperature superconductors. *Phys. Rev. B* **75**, 174506 (2007).
- Chang, J. et al. When low- and high-energy electronic responses meet in cuprate superconductors. *Phys. Rev. B* **75**, 224508 (2007).
- Sala, M. M. et al. Energy and symmetry of dd excitations in undoped layered cuprates measured by cu l3 resonant inelastic x-ray scattering. *New J. Phys.* **13**, 043026 (2011).
- Peng, Y. Y. et al. Influence of apical oxygen on the extent of in-plane exchange interaction in cuprate superconductors. *Nat. Phys.* **13**, 1201 (2017).
- Ivashko, O. et al. Damped spin excitations in a doped cuprate superconductor with orbital hybridization. *Phys. Rev. B* **95**, 214508 (2017).
- Chen, C. T. et al. Out-of-plane orbital characters of intrinsic and doped holes in $\text{La}_{2-x}\text{Sr}_x\text{CuO}_4$. *Phys. Rev. Lett.* **68**, 2543–2546 (1992).
- Hozoi, L. et al. Ab initio determination of Cu 3d orbital energies in layered copper oxides. *Sci. Rep.* **1**, 65 (2011).
- Bishop, C. B. et al. On-site attractive multiorbital hamiltonian for d -wave superconductors. *Phys. Rev. B* **93**, 224519 (2016).
- Yoshida, T. et al. Systematic doping evolution of the underlying Fermi surface of $\text{La}_{2-x}\text{Sr}_x\text{CuO}_4$. *Phys. Rev. B* **74**, 224510 (2006).
- Chang, J. et al. Anisotropic breakdown of Fermi liquid quasiparticle excitations in overdoped $\text{La}_{2-x}\text{Sr}_x\text{CuO}_4$. *Nat. Commun.* **4**, 2559 (2013).
- Zhou, X. J. et al. High-temperature superconductors: universal nodal fermi velocity. *Nature* **423**, 398–398 (2003).
- Zhang, Y. et al. Orbital characters of bands in the iron-based superconductor $\text{BaFe}_{1.85}\text{Co}_{0.15}\text{As}_2$. *Phys. Rev. B* **83**, 054510 (2011).
- White, S. R. & Scalapino, D. J. Competition between stripes and pairing in a $t - t' - J$ model. *Phys. Rev. B* **60**, R753–R756 (1999).
- Maier, T. et al. d -wave superconductivity in the hubbard model. *Phys. Rev. Lett.* **85**, 1524–1527 (2000).
- Laliberté, F. et al. Fermi-surface reconstruction by stripe order in cuprate superconductors. *Nat. Commun.* **2**, 432 (2011).
- Uchida, M. et al. Orbital characters of three-dimensional fermi surfaces in $\text{Eu}_{2-x}\text{Sr}_x\text{NiO}_4$ as probed by soft-x-ray angle-resolved photoemission spectroscopy. *Phys. Rev. B* **84**, 241109 (2011).
- Uchida, M. et al. Pseudogap of metallic layered nickelate $\text{R}_{2-x}\text{S}_x\text{NiO}_4$ ($R = \text{Nd, Eu}$) crystals measured using angle-resolved photoemission spectroscopy. *Phys. Rev. Lett.* **106**, 027001 (2011).
- Lipscombe, O. J. et al. Persistence of high-frequency spin fluctuations in overdoped superconducting $\text{La}_{2-x}\text{Sr}_x\text{CuO}_4$ ($x = 0.22$). *Phys. Rev. Lett.* **99**, 067002 (2007).
- Radaelli, P. G. et al. Structural and superconducting properties of $\text{La}_{2-x}\text{Sr}_x\text{CuO}_4$ as a function of Sr content. *Phys. Rev. B* **49**, 4163–4175 (1994).
- Månsson, M. et al. On-board sample cleaver. *Rev. Sci. Instrum.* **78**, 076103 (2007).
- Strocov, V. N. et al. Soft-X-ray ARPES facility at the ADDRESS beamline of the SLS: Concepts, technical realisation and scientific applications. *J. Synchrotron Radiat.* **21**, 32–44 (2014).
- P. Blaha, K. Schwarz, G. Madsen, D. Kvasnicka and J. Luitz, WIEN2k, An Augmented Plane Wave + Local Orbitals Program for Calculating Crystal Properties. Technische Universität Wien (2001).
- Perdew, J. P., Burke, K. & Ernzerhof, M. Generalized gradient approximation made simple. *Phys. Rev. Lett.* **77**, 3865–3868 (1996).
- Wang, S. et al. Strain derivatives of T_c in $\text{HgBa}_2\text{CuO}_{4+\delta}$: the CuO_2 plane alone is not enough. *Phys. Rev. B* **89**, 024515 (2014).
- Vishik, I. M. et al. Angle-resolved photoemission spectroscopy study of $\text{HgBa}_2\text{CuO}_{4+\delta}$. *Phys. Rev. B* **89**, 195141 (2014).
- Platé, M. et al. Fermi surface and quasiparticle excitations of overdoped $\text{Tl}_2\text{Ba}_2\text{CuO}_{6+\delta}$. *Phys. Rev. Lett.* **95**, 077001 (2005).
- Peets, D. C. et al. $\text{Tl}_2\text{Ba}_2\text{CuO}_{6+\delta}$ brings spectroscopic probes deep into the overdoped regime of the high- T_c cuprates. *New J. Phys.* **9**, 28 (2007).
- Flechsiger, U., Patthey, L. & Schmidt, T. Performance measurements at the SLS spectroscopy beamline. *AIP Conf. Proc.* **705**, 316 (2004).
- Strocov, V. N. et al. High-resolution soft X-ray beamline ADDRESS at the Swiss Light Source for resonant inelastic X-ray scattering and angle-resolved photoelectron spectroscopies. *J. Synchrotron Radiat.* **17**, 631–643 (2010).

Acknowledgements

D.S., D.D., L.D., T.N., C.E.M., C.G.F. and J.C. acknowledge support by the Swiss National Science Foundation. Further, Y.S. and M.M. are supported by the Swedish Research Council (VR) through a project (BIFROST, dnr.2016-06955). O.T. acknowledges support from the Swedish Research Council as well as the Knut and Alice Wallenberg foundation. This work was performed at the SIS, ADDRESS and I05 beamlines at the Swiss Light Source and at the Diamond Light Source. A.M.C. wishes to thank the Aspen Center for Physics, which is supported by National Science Foundation grant PHY-1066293, for hosting during some stages of this work. We acknowledge Diamond Light Source for access to beamline I05 (proposal SI10550-1) that contributed to the results presented here and thank all the beamline staff for technical support.

Author contributions

S.P., T.T., H.T., T.K., N.M., M.O., O.J.L. and S.M.H. grew and prepared single crystals. C.E.M., D.S., L.D., M.H., D.D., C.G.F., K.H., J.C., M.S., O.T., M.K., V.N.S., T.S., P.D., M.H., M.M. and Y.S. prepared and carried out the ARPES experiment. C.E.M., K.H. and J.C. performed the data analysis. C.E.M. carried out the DFT calculations and A.M.C., C.E.M. and T.N. developed the tight-binding model. All authors contributed to the manuscript.

Additional information

Supplementary Information accompanies this paper at <https://doi.org/10.1038/s41467-018-03266-0>.

Competing interests: The authors declare no competing interests.

Reprints and permission information is available online at <http://npg.nature.com/reprintsandpermissions/>

Publisher's note: Springer Nature remains neutral with regard to jurisdictional claims in published maps and institutional affiliations.



Open Access This article is licensed under a Creative Commons Attribution 4.0 International License, which permits use, sharing, adaptation, distribution and reproduction in any medium or format, as long as you give appropriate credit to the original author(s) and the source, provide a link to the Creative Commons license, and indicate if changes were made. The images or other third party material in this article are included in the article's Creative Commons license, unless indicated otherwise in a credit line to the material. If material is not included in the article's Creative Commons license and your intended use is not permitted by statutory regulation or exceeds the permitted use, you will need to obtain permission directly from the copyright holder. To view a copy of this license, visit <http://creativecommons.org/licenses/by/4.0/>.

© The Author(s) 2018